Spin-torque oscillation in a magnetic insulator probed by a single-spin sensor

H. Zhang,[1,2,*] M. J. H. Ku,[1,2,3,*,†] F. Casola,[1,2] C. H. R. Du,[2,‡] T. van der Sar,[2,§] M. C. Onbasli,[4,5] C. A. Ross,[4] Y. Tserkovnyak,[6] A. Yacoby,[2,7] and R. L. Walsworth[1,2,3,8,9,10,¶]

[1]*Harvard-Smithsonian Center for Astrophysics, Cambridge, Massachusetts 02138, USA*
[2]*Department of Physics, Harvard University, Cambridge, Massachusetts 02138, USA*
[3]*Quantum Technology Center and Institute for Research in Electronics and Applied Physics, University of Maryland, College Park, Maryland 20742, USA*
[4]*Department of Materials Science and Engineering, Massachusetts Institute of Technology, Cambridge, Massachusetts 02139, USA*
[5]*Koç University, Department of Electrical and Electronics Engineering, Sarıyer, 34450 Istanbul, Turkey*
[6]*Department of Physics and Astronomy, University of California, Los Angeles, California 90095, USA*
[7]*John A. Paulson School of Engineering and Applied Sciences, Harvard University, Cambridge, Massachusetts 02138, USA*
[8]*Center for Brain Science, Harvard University, Cambridge, Massachusetts 02138, USA*
[9]*Department of Physics, University of Maryland, College Park, Maryland 20742, USA*
[10]*Department of Electrical and Computer Engineering, University of Maryland, College Park, Maryland 20742, USA*

(Received 11 December 2018; revised 4 May 2020; accepted 6 May 2020; published 2 July 2020)

We locally probe the magnetic fields generated by a spin-torque oscillator (STO) in a microbar of ferrimagnetic insulator yttrium-iron-garnet using the spin of a single nitrogen-vacancy (NV) center in diamond. The combined spectral resolution and sensitivity of the NV sensor allows us to resolve multiple spin-wave modes and characterize their damping. When damping is decreased sufficiently via spin injection, the modes auto-oscillate, as indicated by a strongly reduced linewidth, a diverging magnetic power spectral density, and synchronization of the STO frequency to an external microwave source. These results open the way for quantitative, nanoscale mapping of the microwave signals generated by STOs, as well as harnessing STOs as local probes of mesoscopic spin systems.

DOI: 10.1103/PhysRevB.102.024404

I. INTRODUCTION

Coherent, self-sustained oscillation of magnetization induced by spin-torque [1–7] is a promising source for on-chip, nanoscale generation of microwave magnetic fields. Such spin-torque oscillators (STOs) have been proposed as on-chip sources of spin waves (SWs) [2], as nanoscale microwave generators [2–4], and as building blocks in neural networks [2,3,5]. While optical methods [7–10] such as Brillouin light scattering and magneto-optical Kerr effect microscopy have been used to spatially investigate the magnetization dynamics of STOs, the detection of on-chip STO microwave fields with a probe that allows nanoscale spatial imaging and sub-MHz spectral resolution has remained an outstanding challenge.

Recently, the electron spin associated with the nitrogen-vacancy (NV) defect in diamond has emerged as a sensitive magnetic-field sensor [11] that allows nanoscale spatial resolution [12,13], sub-Hz spectral resolution [14], and excellent magnetic-field sensitivity [15]. In this work, we use single NV magnetometry to study the local magnetic fields generated by an STO in a yttrium-iron-garnet (YIG) microbar that can be driven into auto-oscillation by a spin-current injected via the spin-Hall effect in a platinum thin film [6,8,16]. We present multiple signatures of STOs as detected by the NV sensor. The techniques developed here can also be employed in scanning NV microscopy for nanoscale imaging of STO microwave fields.

II. METHODS

The experimental setup is based on a home-built laser scanning confocal microscope, which has been described previously [13]. As part of the experimental sensing platform, we pattern bulk diamond containing NVs into a nanobeam structure [17–19]. To locally detect the STO magnetic fields, we position a diamond nanobeam containing an individually addressable NV sensor at ∼100 nm from a Pt (10 nm)/YIG (17 nm) hybrid microstructure ($2.5 \times 9\ \mu m^2$ in dimension) [Fig. 1(a)]. Au electrical leads supply the DC current I_{dc} to the Pt wire for spin injection. A nearby Au stripline [Fig. 1(b)] delivers microwave signals for both control of the NV spin state and for microwave-driving of spin-wave modes in the YIG bar. Further information on NV physics relevant to sensing of magnetic fields can be found in Refs. [11–15,20–23],

*These authors contributed equally to this work.
†Present address: Department of Physics and Astronomy, University of Delaware, Newark, Delaware 19716, USA.
‡Present address: Department of Physics, University of California San Diego, La Jolla, California 92093, USA.
§Present address: Kavli Institute of Nanoscience, Delft University of Technology, 2628CJ Delft, Netherlands.
¶walsworth@umd.edu

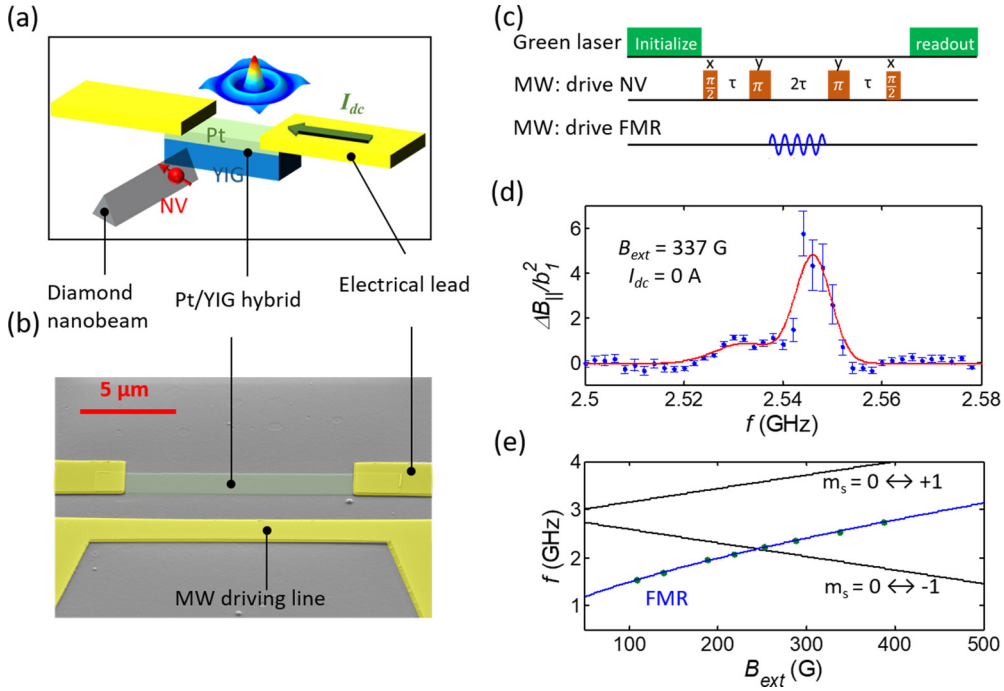

FIG. 1. (a) Schematic illustration of the device: a diamond nanobeam containing a single NV spin is positioned near a hybrid Pt/YIG structure. (b) Scanning electron micrograph of the device (before positioning the diamond nanobeam). (c) NV optical (green) and microwave (red) spin-echo sequence for stray-field magnetometry of spin-wave resonances. A spin-wave (FMR) drive is applied during the central free-precession period. A change in the YIG stray field $\Delta B_{||}$ imparts a phase on the NV spin state and is read out via spin-dependent photoluminescence. A free precession time $\tau \approx 5.5\,\mu$s is used for such stray-field magnetometry. (d) Example of YIG spin-wave resonances measured with the pulse sequence in (c), at applied static magnetic field $B_{\rm ext} = 337$ G aligned with the NV axis. Plotted is the NV-measured stray static magnetic field along the NV axis, $\Delta B_{||}$, as a function of the spin-wave drive frequency. The signal is normalized by the square of the drive field b_1^2, which is proportional to the spin-wave drive power and is independently measured on-chip using the same NV sensor [20]. Blue dots: data. Red line: double Gaussian fit, yielding FWHM = 8.5(6) MHz for the dominant mode attributed to the spatially homogeneous ($n = 1$) ferromagnetic resonance (FMR) of the YIG bar. (e) Green dots: Magnetic-field ($B_{\rm ext}$) dependence of the fundamental spin-wave resonance frequency extracted from fits to measurements such as shown in (d). Blue line: fit reveals characteristic Kittel-like behavior of FMR. Black lines: NV transition frequencies corresponding to the $m_s = 0 \leftrightarrow \pm 1$ transitions. NV-spin manipulation pulses are applied on the $m_s = 0 \leftrightarrow +1$ transition.

and details of the fabrication processes can be found in Appendix A.

III. RESULTS AND DISCUSSIONS

A. NV stray field measurement of ferromagnetic resonance (FMR)

We begin by probing the spin-wave spectrum of the YIG micro-magnet using microwave excitation. We sweep the frequency of a microwave drive field and use the NV spin sensor to detect changes in the stray static magnetic field $\Delta B_{||}$ ($||$ denotes the projection onto NV quantization axis) due to changes in the YIG magnetization upon exciting a spin-wave resonance [20]. Figure 1(c) depicts the sensing sequence, and Fig. 1(d) shows the spectrum at zero DC current. We observe multiple spectral peaks, the most prominent of which persists as the strongest mode throughout the entire sweep range of the external magnetic field $B_{\rm ext}$. We attribute this peak to the spatially homogeneous ($n = 1$) ferromagnetic resonance (FMR) of the YIG bar as it couples efficiently to our microwave drive field. The center frequency of this mode vs $B_{\rm ext}$ follows a Kittel-like dependence [Fig. 1(e)].

B. NV detection of damping control with spin current

Next, we demonstrate control of spin-wave resonance damping by injecting a spin current into the YIG via the Pt contact. As illustrated in Fig. 2(a), the effect of a spin current on the dynamics of the magnetization can be described as a spin-orbit torque acting on the YIG magnetization [24]. Depending on the relative orientation between the injected spins and the equilibrium magnetization, the spin-orbit torque can either reduce or enhance the effective damping of precessional motion of the magnetization vector (see Appendix B for further explanation). We observe such damping modification by measuring the response of the YIG stray field to the microwave drive as a function of $I_{\rm dc}$. In Fig. 2(b), we show example FMR spectra of the YIG stray field $\Delta B_{||}$, normalized by the square of the microwave drive amplitude b_1^2, as a function of the drive frequency at several $I_{\rm dc}$. A strong dependence of the peak amplitude on $I_{\rm dc}$ indicates that damping is reduced (enhanced) for positive (negative) $I_{\rm dc}$.

When the intrinsic magnetic damping is compensated by the antidamping torque exerted by the injected spin current, we expect an increase in the rate of change of the FMR peak amplitude as a function of the microwave drive

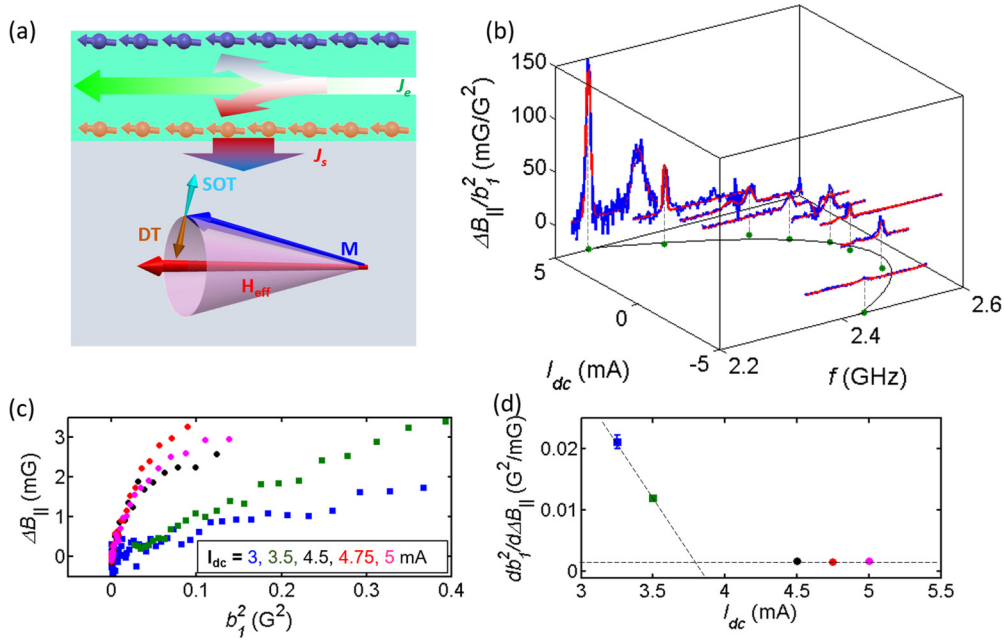

FIG. 2. (a) Sketch of the magnetization dynamics of the Pt/YIG device under the influence of a spin current. The electrical current ($\mathbf{J_e}$) injects a spin current ($\mathbf{J_s}$) into the YIG, leading to a spin-orbit torque (labeled SOT) that either reduces or enhances magnetic damping depending on the relative orientation between the injected spins and the magnetization $\mathbf{M}$. DT denotes the (intrinsic) damping torque. (b) NV-measured, microwave-driven spin-wave resonance spectra in the YIG as a function of the DC current I_{dc} through the Pt. [Measurement sequence shown in Fig. 1(c)]. Blue traces: normalized change in YIG stray field $\Delta B_{||}/b_1^2$ as a function of microwave driving frequency for $I_{dc} = 5, 4, 3, 2, 1, 0, -2, -5$ mA. Red lines: double Gaussian fit to data. Green dots: center frequency of the fundamental spin-wave mode vs. I_{dc}. Black curve: parabolic fit to green dots. (c) On-resonance $\Delta B_{||}$ as a function of microwave driving power b_1^2 for different values of I_{dc}. Black, red, and pink dots correspond to $I_{dc} = 4.5$, 4.75, and 5 mA, for which the initial slopes ($d\Delta B_{||}/db_1^2$) have no discernable difference. Blue and green squares correspond to $I_{dc} = 3$ and 3.5 mA, for which initial slopes are significantly smaller. (d) Plot of the inverse of the initial slopes, i.e., $db_1^2/d\Delta B_{||}$, as a function of I_{dc}. Diagonal and horizontal dashed lines serve as eye guide to illustrate that there exists a current threshold as onset of an auto-oscillating spin torque oscillator (STO).

power. Figure 2(c) plots the on-resonance peak amplitude of $\Delta B_{||}$, extracted from data such as those in Fig. 2(b), as a function of the microwave drive power b_1^2 at different I_{dc}. We observe two distinct regimes: for $I_{dc} \lesssim 4$ mA, the peak amplitude increases approximately linearly over a large range of microwave drive power, while for $I_{dc} \gtrsim 4$ mA, the signal increases sharply first and then saturates. The distinction between these two regimes is more evident in Fig. 2(d), which plots the inverse of the initial slopes of $\Delta B_{||}$ vs b_1^2 (i.e., $db_1^2/d\Delta B_{||}$) as a function of I_{dc}. The trend of the inverse on-resonance slopes quantifies the evolution of the effective damping coefficient α_{eff}, which monotonically changes with $(1/\chi'')^2 \propto (b_1/m)^2 \sim db_1^2/d\Delta B_{||}$, where χ'' is the imaginary part of the YIG bar's magnetic susceptibility, and m is the oscillation amplitude of the transverse magnetization [25]. In Fig. 2(d) we observe $db_1^2/d\Delta B_{||}$ decreases as a function of I_{dc} (diagonal dashed line) until a certain threshold, after which it plateaus (horizontal dashed line). We interpret the plateau to be due to auto-oscillation of a STO, with the crossing of the dashed lines corresponding to the STO onset threshold current ~ 3.8 mA. Note that this threshold current value agrees well with an independent estimate obtained from Fig. 5(a).

C. Effect of enhanced magnetic fluctuation due to spin injection on effective saturation magnetization

Spin injection is expected to increase magnetic noise [4], which leads to a decrease of the effective saturation magnetization (M_e). One way to verify this expectation is to measure the resulting fundamental mode frequency shift [26]. However temperature change will also affect M_e. To distinguish the effect of spin injection induced magnetic noise enhancement from a temperature effect (Joule heating), only limited efforts have been made: one example is an indirect measurement via pulsing the injection current [26]. A more direct and accurate method is desirable.

We extract temperature change as a function of I_{dc} by measuring the NV ground state zero-field splitting [27]; the results are shown in Fig. 3(a) as blue dots. From Fig. 2(b), we can extract FMR center frequencies for different injection currents; the results are shown in Fig. 3(b) as green dots. According to the Néel model [28], M_e can be inferred from temperature measurements. Furthermore, with an established relationship between temperature and I_{dc} [Fig 3(a)], we can extract the saturation magnetization at room temperature M_s (Appendix C). We show M_e/M_s extracted from the temperature measurement as a function of I_{dc} as blue dots in Fig. 3(c).

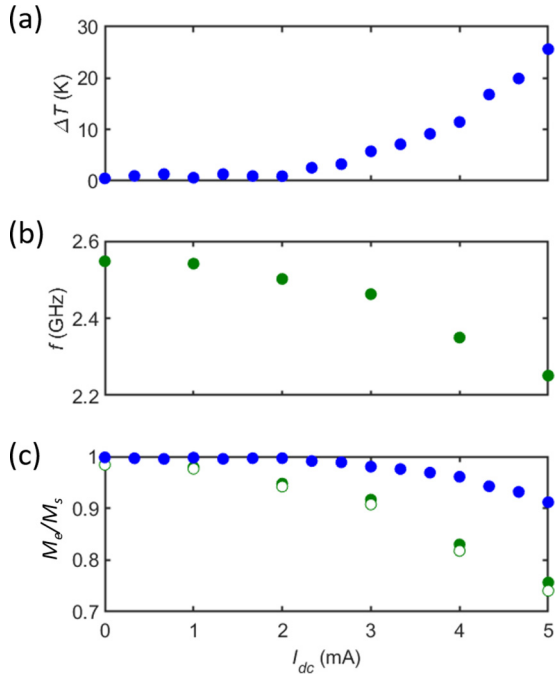

FIG. 3. (a) Blue dots show temperature, measured with NV, changes with $I_{\rm dc}$. (b) Green dots represent center frequencies of fundamental SW mode at different $I_{\rm dc}$ measured by NV stray-field magnetometry measurements [extracted from Fig. 2(b)]. (c) Normalized effective saturation magnetization (M_e/M_s) as a function of $I_{\rm dc}$: data shown as blue dots are derived from temperature measurements. Data shown as solid green dots are from FMR center frequency measurements without correction to remove impact from Oersted field, while data shown as open green circles are corrected.

On the other hand, M_e can also be directly extracted from the FMR center frequency, shown as solid green dots in Fig 3(c). To account for any effect from the Oersted field generated by the current in Pt, a correction is performed by measuring the Oersted field with optically detected magnetic resonance (ODMR) measurements [15]. The green open circles in Fig. 3(c) show the calculated M_e/M_s with such a correction. Note that values for M_e/M_s inferred from the temperature and FMR center frequency methods are significantly different. This difference sets an upper bound for the magnetic noise enhancement from spin injection; also our result qualitatively agrees with previous observations [26]. We note here that we cannot rule out temperature measurement inaccuracy due to the thermal resistance between the diamond beam and Pt metal. Nevertheless, our measurements give an upper bound estimate for the magnetic noise enhancement. A future study will be needed to improve the accuracy of NV temperature measurements. With modest improvements, the temperature measurement capability of NV sensors will provide another powerful diagnostic tool to gain deeper insights of STO physics.

D. STO measured with NV spin-relaxometry

To study auto-oscillation of the spin-wave modes in the YIG bar, we characterize the power spectral density of the magnetic noise generated by the modes as a function of $I_{\rm dc}$ and in the absence of microwave excitation. This measurement is motivated by evidence of enhanced magnetic fluctuations with spin injection, presented in the previous section. We use the NV spin as a field-tunable spectrometer via a technique known as NV spin-relaxometry [20], where the NV spin relaxation rates Γ are measured to quantify the magnetic-noise power spectral density $B^2(\omega)$ at the NV $m_s = 0 \leftrightarrow \pm 1$ transition frequencies $\omega_\pm = 2\pi(D_{\rm gs} \pm \gamma B_{\rm ext})$ via the relation $\Gamma_\pm = \frac{\gamma^2}{2} B^2(\omega_\pm)$. Here, $D_{\rm gs} = 2.87$ GHz is the NV zero-field splitting and $B_{\rm ext}$ is the external static magnetic field aligned with the NV axis. To characterize NV spin relaxation, we prepare the NV spin in the $m_s = 0$ state and determine the spin-relaxation rate Γ in the presence of YIG bar magnetic noise by measuring the spin-dependent photoluminescence $PL(\tau, \omega) = PL(\tau = 0)e^{-\Gamma(\omega)\tau}$ after a hold time τ [Fig. 4(a)]. In Fig. 4(b), we show an example NV spin-relaxometry experiment at $I_{\rm dc} = 5.8$ mA, where we measure the photoluminescence (PL) at a fixed τ as we vary the external magnetic field that sweeps the lower transition frequency ω_- over several spin-wave resonances. In this situation, the rate $\Gamma \approx \Gamma_-$; Γ_+ is negligible as the density of thermal magnons is suppressed at energy ω_+, which is far detuned from spin-wave resonances. The magnetic field fluctuations produced by the different YIG spin-wave modes increase the NV spin relaxation rate, which results in decreased NV PL [29,30]. By performing this measurement at multiple $I_{\rm dc}$, we map the noise spectrum of spin-waves as a function of $B_{\rm ext}$ and $I_{\rm dc}$ [Fig. 4(c)]. The red/blue stars denote the locations of prominent spin-wave resonances (obtained by fitting the peak centers at each $I_{\rm dc}$), which we call $\rm STO_1$ and $\rm STO_2$. We identify $\rm STO_1$ as the spatially homogeneous ($n = 1$) FMR and $\rm STO_2$ as a higher order ($n = 2$) spin-wave mode (Appendix D). The spectral resolution of the NV sensor ($\lesssim$1 MHz) allows us to zoom in closely on the regions where the two spin waves approach each other [Figs. 4(d) and 4(e)], and observe what seems to be a mode anticrossing, hinting at hybridization of the spin-wave modes due to mode interactions. Micromagnetic simulations elucidate the nature of the modes and point to the possibility of mode mixing (Appendix D). We estimate a mode coupling strength of about 10 MHz (Appendix E), which is larger than the linewidth of the individual modes [see Fig. 5(b)].

To study quantitatively the power spectral density of the magnetic field noise generated by $\rm STO_1$ and $\rm STO_2$, we tune the NV transition frequency into resonance with the modes by adjusting $B_{\rm ext}$; and then extract the NV spin relaxation rate Γ as a function of $I_{\rm dc}$ [Fig. 5(a)]. As we change $I_{\rm dc}$, we observe a dramatic increase in the STO magnetic-noise power spectral density of up to three orders of magnitude, a key signature of auto-oscillation [31]. The inset of Fig. 5(a) maps $1/\Gamma = T_1$ as a function of $I_{\rm dc}$; and we use the intersection of a linear fit of $1/\Gamma$ at low current with $1/\Gamma = 0$ to indicate the onset (threshold) of auto-oscillation, following the relation [32,33] $1/\Gamma \propto 1/p \propto 1 - I_{dc}/I_{th}$, where p is the peak power spectral density emitted by the STO and I_{th} is the threshold current. For $\rm STO_1$, we estimate $I_{th1} \approx 3.5$ mA, close to the estimate made above from the stray-field magnetometry measurements in Fig. 2(d). For $\rm STO_2$, we obtain a higher threshold current $I_{th2} \approx 4.4$ mA. A strong correlation between linewidth reduction [Fig. 5(b)] and divergence of magnetic fluctuations [Fig. 5(a)] is consistent with Landau-Lifshitz-Gilbert phenomenology: that is,

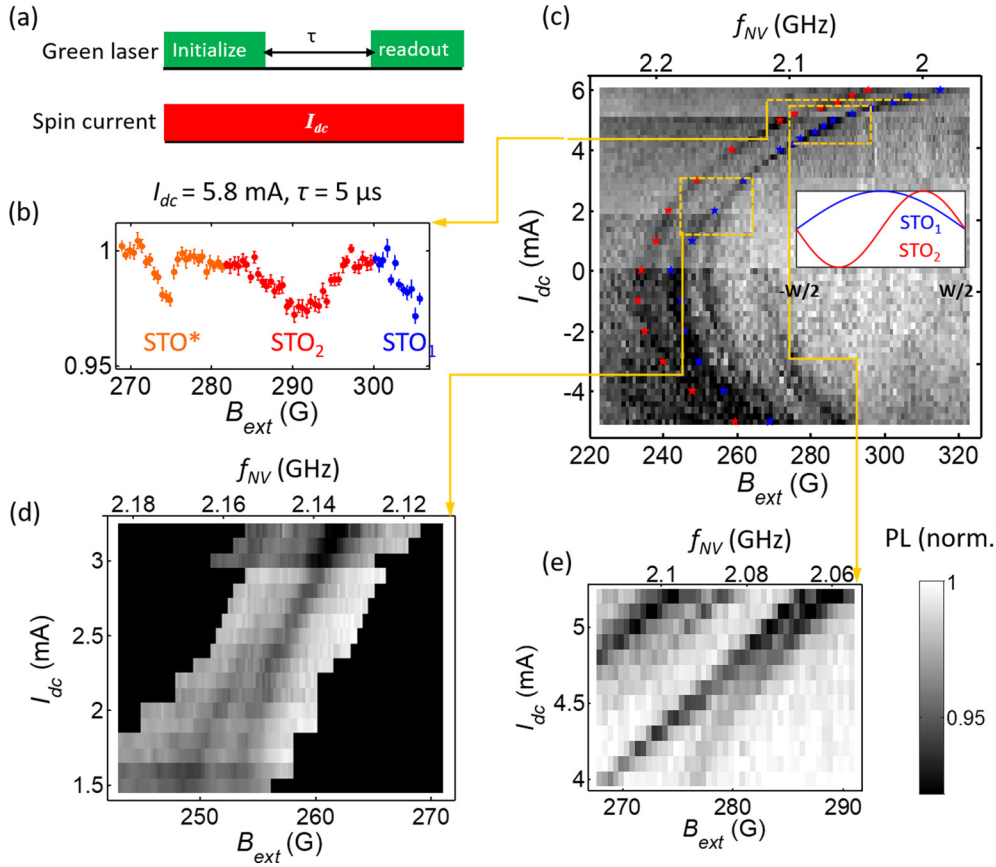

FIG. 4. (a) NV spin-relaxometry measurement sequence. The NV spin is initialized into $m_s = 0$ by a green laser pulse and let to relax for a time τ, after which the spin population is characterized via the spin-dependent PL during a laser readout pulse. Noise that is resonant with an NV transition frequency causes NV spin relaxation. (b) NV spin-relaxometry measurement at $I_{dc} = 5.8$ mA and $\tau = 5\,\mu$s. By tuning the magnetic field B_{ext}, the frequency of the $m_s = 0 \leftrightarrow -1$ transition is swept over three spin-wave (SW) modes in the YIG, whose field-noise causes strong NV spin relaxation and thus dips in the normalized PL signal. (c) Performing the measurement shown in panel (b) for different I_{dc} yields a 2D plot of PL *vs* I_{dc} and B_{ext} that displays the presence and dispersion of spin-torque oscillators (STOs) in the system. Different delay times τ of 150, 50, 15, 5, and 3 μs are used for the different I_{dc} ranges of [−5 mA:0 mA], [0.2 mA:1.8 mA], [2 mA:3 mA], [3.2 mA:5 mA], and [5.2 mA:6 mA], respectively. Top horizontal axis shows the $m_s = 0 \leftrightarrow -1$ transition frequency at corresponding B_{ext}. Blue stars indicate fits of peak centers for the first resonance on the right-hand-side (STO$_1$), while red stars are fits of peak centers for the second (STO$_2$). These two STOs are also indicated in panel (b). Note that an additional oscillator [data points are orange in color and designated as STO* in panel (b)] appears when $I_{dc} = 5.8$ mA and persists for higher current. Inset illustrates mode spatial distribution of STO$_1$ and STO$_2$ along width of Pt/YIG microstructure (W). (d) and (e). Zoomed-in, high-resolution views of (c), where spin-wave modes are observed to approach each other.

the spin-orbit torque reduces the damping torque and the associated STO linewidth. As we increase I_{dc} further, we surprisingly observe a reduction in the power spectral density accompanied by linewidth broadening and the appearance of a higher-order STO [STO* as shown in Fig. 4(b)]. This observation may imply that strong spin injection introduces an additional magnon decay channel, with the magnetic system approaching a rethermalization scenario [34], though we leave a study of this phenomenon to future work.

E. NV characterization of STO synchronized to external microwave source

Finally, we demonstrate that the Pt/YIG STO can be synchronized with an external microwave source, as observed previously for STOs in metallic ferromagnets [34,35]. We use the measurement scheme shown in Fig. 6(a), which is an NV spin-relaxometry measurement with an added microwave drive field. We sweep the frequency f_{MW} of this drive field around the free-running STO frequency. By monitoring the magnetic-noise power spectral density at the NV transition frequency, we observe locking of the STO over a frequency interval Δf_s [Fig. 6(b)]. Figures 6(c) and 6(d) show that the locking interval increases approximately linearly with the drive amplitude b_1 as expected for frequency-locked oscillators. We observe an increase of the synchronization bandwidth for larger I_{dc} [Fig. 6(d)]. Frequency locking to an external microwave source can be used to quickly tune the STO in and out of resonance with the control frequency of a target system.

IV. CONCLUSION

In summary, we used the spin of a single NV center in diamond as a nanoscale magnetic sensor to measure the local magnetic fields generated by STOs driven by spin-current in a Pt/YIG hybrid microstructure. We demonstrated STO

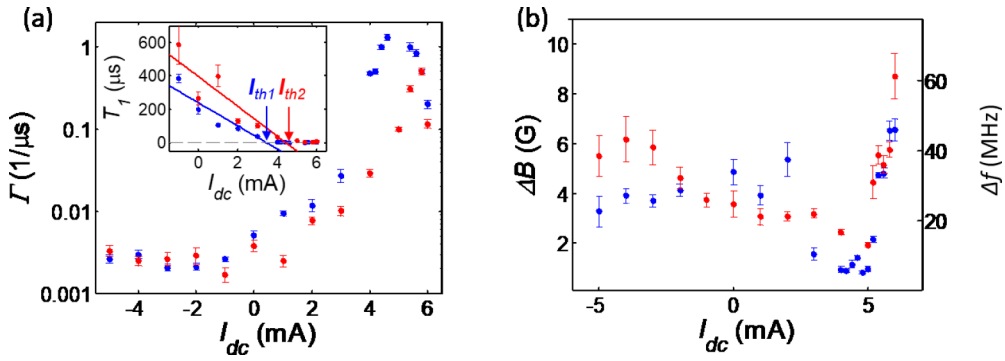

FIG. 5. (a) NV spin relaxation rate (Γ) is measured at the current and magnetic field values indicated by the blue and red stars in Fig. 4(c), where the spin-torque oscillators (STOs) are resonant with the $m_s = 0 \leftrightarrow -1$ transition frequency. At each of these current and magnetic field values, we sweep τ, perform an NV spin-relaxometry measurement sequence [Fig. 4(a)], and extract the exponential decay time constant Γ. Γ_{STO1} (red) and Γ_{STO2} (blue) are plotted as a function of I_{dc}. The dramatic order-of-magnitude increase of the relaxation rate above $I_{dc} \sim 3$ mA indicates spin-torque induced auto-oscillation of the STOs. Inset shows $1/\Gamma = T_1$ vs I_{dc} for both STOs. Linear fits at low current ($I_{dc} < 4$ mA) intersect with $T_1 = 0$ at $I_{th1} = 3.5$ mA and $I_{th2} = 4.4$ mA, which we define as the auto-oscillation threshold currents. (b) Measured STO linewidth ΔB as a function of I_{dc} for STO_1 (blue dots) and STO_2 (red dots). The vertical axis on the right gives the linewidth in frequency (MHz), calculated from ΔB using the Kittel relation at $B_{ext} \sim 250$ G and $I_{dc} = 0$.

auto-oscillation [6] in this magnetic insulator using three independent methods: suppression of the effective damping torque, divergence of the power spectral density at the STO frequency, and STO synchronization to an external microwave source.

NV magnetometry provides a useful combination of high spectral resolution, good sensitivity, nanoscale spatial resolution, and applicability to a wide range of samples and operating conditions [36]. The NV spin-relaxometry technique, used in the present experiment, has a spectral resolution $\lesssim$1 MHz, set by the NV spin dephasing rate [22]. In other recent results, sub-Hz NV resolution has been realized using synchronized readout [14]; or can be enabled via modest cooling [21]. Thus in future work, NV sensors should be able to probe the sub-Hz

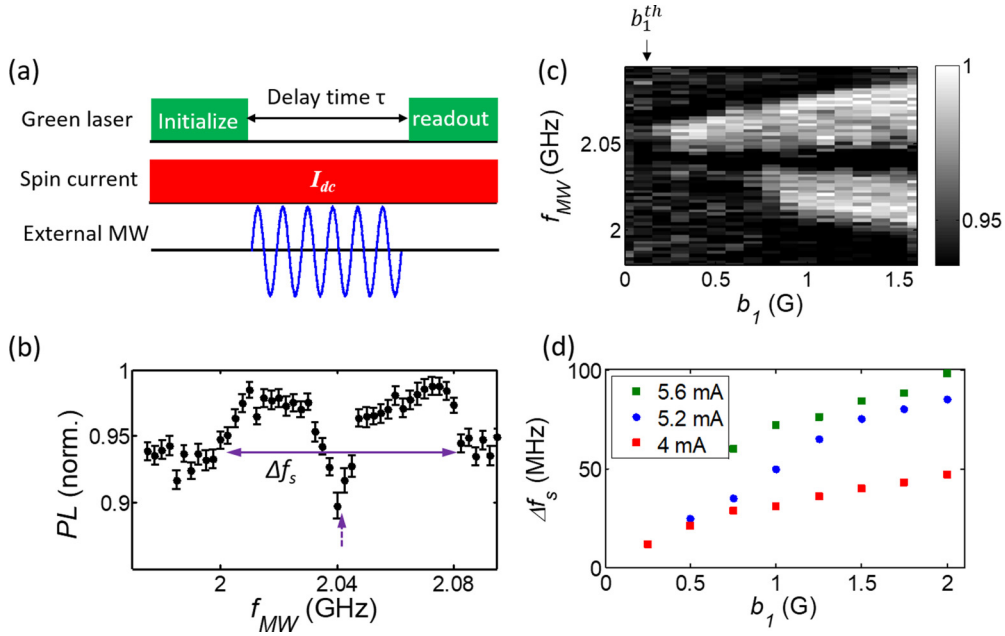

FIG. 6. (a) NV spin-relaxometry measurement sequence as in Fig. 4(a), with added MW drive. For synchronization measurement, B_{ext} is tuned such that the NV $m_s = 0 \leftrightarrow -1$ transition coincides with STO resonance. (b) Measured NV photoluminescence (PL) as a function of the MW drive frequency f_{MW}, at $I_{dc} = 5.2$ mA, $B_{ext} = 292$ G, and MW drive amplitude $b_1 = 1.5$ G. When the MW drive is resonant with the NV transition frequency, a dip in the PL is observed because the driving deplete $m_s = 0$ population. Over a frequency interval Δf_s the STO can be locked to the MW drive and thus detuned from the NV transition, thereby decreasing the NV spin relaxation and correspondingly increasing the measured PL. When the MW drive frequency is detuned beyond the locking interval (i.e., synchronization bandwidth), the STO remains resonant with the NV transition frequency, leading to strong NV-spin relaxation and a corresponding reduced PL. (Appendix F for detailed data analysis.) (c) 2D map of PL vs f_{MW} and MW drive amplitude b_1. The synchronization bandwidth increases linearly with b_1. b_1^{th} is the threshold amplitude at which synchronization begins to occur. (d) Synchronization bandwidth vs b_1 at different I_{dc} (4, 5.2, and 5.6 mA).

regime of STO behavior [3], comparable to the capability of state-of-the-art electrical detection [37], combined with nanoscale spatial characterization of STO-generated magnetic fields [12,13], which is unavailable to electrical detection. Spatial mapping at such length scales would provide access to locations of large STO magnetic-field intensity, with the potential to use an STO to drive magnetic excitations in other systems of interest, such as spin waveguides [38] and spin qubits [39]. Finally, studies of spin-torque oscillation may provide insight into phenomena such as magnon thermodynamics [40], strongly correlated many-body physics [22], and control over magnetic phase transitions [41].

ACKNOWLEDGMENTS

The authors acknowledge the provision of diamond samples by Element 6, assistance with nanobeam fabrication from M. Warner and M. Burek, the use of a setup for nanobeam transfer from P. Kim, use of the ion mill facility in the J. Moodera lab, and experimental assistance from K. Arai, M. Han, and J.-C. Jaskula. This material is based upon work supported by, or in part by, the United States Army Research Laboratory and the United States Army Research Office under Contract/Grants No. W911NF1510548 and No. W911NF1110400. A.Y. acknowledges support from the Army Research Office under Grant No. W911NF-17-1-0023. The views and conclusions contained in this document are those of the authors and should not be interpreted as representing the official policies, either expressed or implied, of the Army Research Office or the US Government. The US Government is authorized to reproduce and distribute reprints for Government purposes notwithstanding any copyright notation herein. Work at the Massachusetts Institute of Technology was supported by the Solid-State Solar-Thermal Energy Conversion Center (S3TEC), an Energy Frontier Research Center funded by DOE, Office of Science, and BES under Award No. DE-SC0001299/DE-FG02-09ER46577. Work at the University of California, Los Angeles, is supported by the US Department of Energy (DOE), Office of Basic Energy Sciences (BES) under Award No. DE-SC0012190. F.C. acknowledges support from the Swiss National Science Foundation Grant No. P300P2-158417. This research is also funded in part by the Gordon and Betty Moore Foundation's EPiQS Initiative through Grant No. GBMF4531, the STC Center for Integrated Quantum Materials, National Science Foundation (NSF) Grant No. DMR-1231319, and by the National Science Foundation under Grant No. EFMA-1542807. This work was performed in part at the Center for Nanoscale Systems (CNS), a member of the National Nanotechnology Coordinated Infrastructure Network (NNCI), which is supported by the NSF under NSF Award No. 1541959. CNS is part of Harvard University.

H.Z, M.J.H.K, A.Y., and R.L.W. conceived the project. R.L.W. and A.Y. supervised the project. H.Z. and M.J.H.K developed measurement protocols, built the experimental setup for NV measurement, performed the measurements, and analyzed the data. H.Z. fabricated the Pt/YIG device and performed micromagnetic simulations. F.C. and H.Z. developed the nanobeam platform and fabricated the nanobeams. F.C. helped with micromagnetic simulations. M.C.O. and C.A.R. provided the YIG sample. H.Z., M.J.H.K., T.v.d.S., F.C., C.H.R.D., Y.T., A.Y., and R.L.W. contributed to the interpretation. H.Z., M.J.H.K., T.v.d.S., C.H.R.D., and R.L.W. wrote the manuscript with the help from all coauthors.

APPENDIX A: SAMPLE FABRICATION

Fabrication of the Pt/YIG device starts with a 17-nm YIG film epitaxially grown on a (111) orientation gadolinium–gallium garnet substrate using pulsed laser deposition [42]. A 10-nm layer of platinum (Pt) is sputtered on top of the YIG film, which is first cleaned by an Ar+ plasma at a pressure below 5×10^{-8} Torr to ensure good Pt purity. The Pt/YIG stripe is defined by electron-beam lithography (Elionix F125, 125 kV) with a PMMA (495A2, ∼30 nm)/HSQ (XR-1541-006, ∼250 nm and FOX-16, ∼500 nm) resist stack, followed by developing in 25% TMAH. Ar+ ion milling is used to transfer the pattern onto the substrate and form the Pt/YIG hybrid microstructure. Finally, leads for DC current and microwave driving are defined by electron-beam lithography and e-beam evaporation techniques. See Fig. 7 for further fabrication details. See Fig. 8 for example scanning electron microscope (SEM) images of the devices.

APPENDIX B: SPIN INJECTION AND ITS DEPENDENCE ON ORIENTATION OF EXTERNAL MAGNETIC FIELD, MAGNETIZATION, AND SPIN POLARIZATION

For an NV center, the quantization axis is set by the nitrogen atom and the vacancy along one of the four diamond crystal axes. To perform sensing with a single NV, it is best to align the external magnetic bias field along the NV axis in order to maximize the PL and the contrast between the NV spin states [44]. An NV in a diamond nanobeam can, in principle, be pointing along any direction with respect to the Pt/YIG microstructure because the orientation of the nanobeam is random. As we align the external field $\mathbf{B}_{\text{ext}}$ with the NV axis, the orientation of the field will also affect the efficacy of the generation of spin-orbit torque (SOT).

It is generally accepted that the effect of a pure spin current on the magnetization can be described by the Slonczewski spin-transfer torque or similarly the SOT included in the Landau-Lifshitz-Gilbert equation:

$$\dot{\boldsymbol{M}} = -\gamma \boldsymbol{M} \times \boldsymbol{H}_{\text{eff}} + \frac{\alpha}{M_S} \boldsymbol{M} \times \dot{\boldsymbol{M}} + \frac{\beta}{M_S^2} \boldsymbol{M} \times (\boldsymbol{M} \times \hat{\boldsymbol{s}}).$$

Here, α is the Gilbert damping parameter; β describes the magnitude of SOT, which is proportional to the spin current density $\mathbf{J}_s$; M_s is the saturation magnetization; $\mathbf{M}$ is the dynamic magnetization vector; $\mathbf{H}_{\text{eff}}$ is the total magnetic field, which includes the external bias field $\mathbf{B}_{\text{ext}}$, the Oersted field produced by the DC current, and other field components contributing to a net internal field; and $\hat{\boldsymbol{s}}$ is a unit vector in the direction of the spin current polarization. The second term on the right-hand side can be viewed as a damping torque (DT) and the third term is the SOT. Depending on the relative orientation between the spin current and the external field, the SOT can act either along or against the DT.

Let us assume we send the DC current along the long direction of the Pt/YIG device. We set the coordinate system

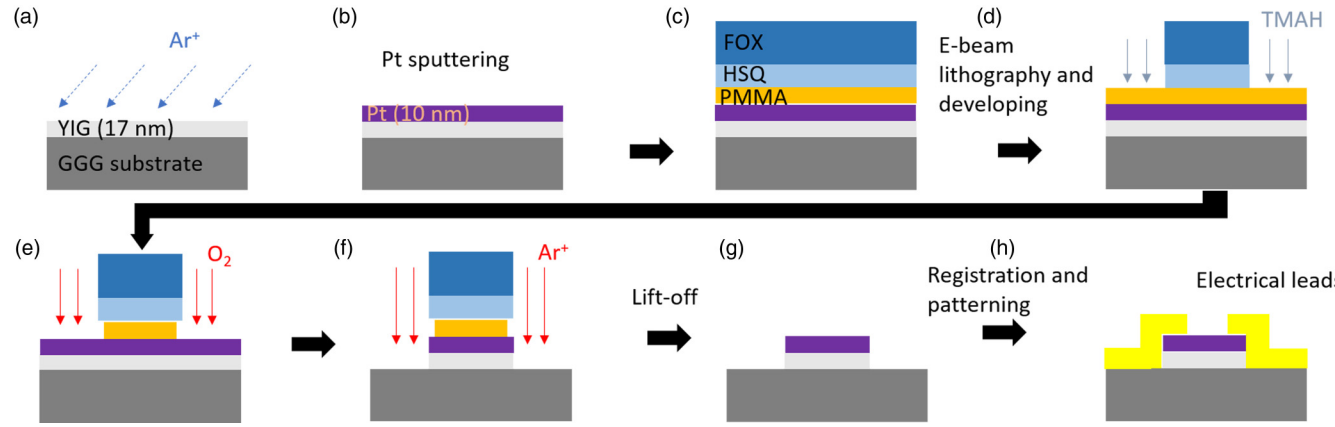

FIG. 7. Pt/YIG hybrid device fabrication processes. (a) Ar^+ plasma cleaning inside sputter chamber. (b) DC sputtering of 10 nm Pt. Note: this procedure has successfully generated Pt/YIG interfaces showing excellent spin mixing conductance [43]. (c) Coating substrate with PMMA/HSQ/FOX resist stack. (d) E-beam lithography and developing in TMAH to form etching mask. (e) O_2 reactive ion etch to remove excessive PMMA and to induce proper undercut. (f) Ar^+ milling to transfer pattern from the etching mask onto the substrate. (g) Lift-off to remove the resist stack. (h) E-beam patterning of electrical leads and MW driving lines with proper alignment with respect to existing Pt/YIG microstructures.

such that the x axis is along the device's long direction, the y axis is pointing along the short direction, and the z axis is along the vertical [see Fig. 9(a)]. Spin-orbit coupling in Pt leads to generation of a spin current $\mathbf{J}_s$ that is orthogonal to the charge current $\mathbf{J}_e$ with the injected spins polarized along $\mathbf{s}$. When spin waves (SWs) are excited, the YIG magnetization $\mathbf{M}$ tilts slightly from the axis set by $\mathbf{B}_{\text{ext}}$ and precesses around this axis. The generation of SOT is most effective when $\mathbf{s}$ is almost parallel with $\mathbf{M}$. Therefore, the best orientation for $\mathbf{B}_{\text{ext}}$ for STO generation is for it to point along the short direction of the Pt/YIG device [Fig. 9(a)].

For the NV employed for single-spin sensing in this work (which we call NV_a), the orientation of this NV and hence $\mathbf{B}_{\text{ext}}$ is shown in Fig. 9(b). The projection of the external field to the short direction of the device is large, $\sim 0.72|\mathbf{B}_{\text{ext}}|$, and therefore we can align the external field along the NV axis while still maintaining effective generation of SOT.

Another NV (referred to as NV_b) is present in the diamond nanobeam, with orientation as shown in Fig. 9(c). In contrast to NV_a, NV_b is almost vertical, and when $\mathbf{B}_{\text{ext}}$ is aligned with this NV, the efficacy of SOT generation is adversely affected. The effect of weaker SOT generation can be

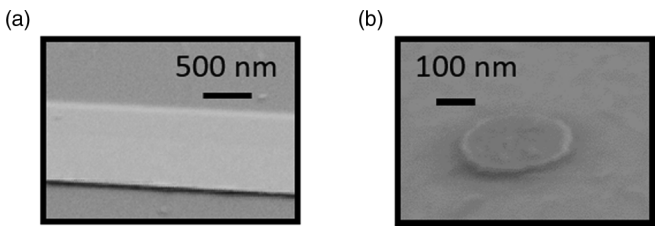

FIG. 8. (a) SEM image of Pt/YIG hybrid shows smooth edge. Throughout the fabrication process, extra care is taken to preserve material quality, e.g., only mild solvents are used. (b) SEM image of an example YIG disc (~400 nm in diameter), fabricated with the use of high-resolution e-beam resist.

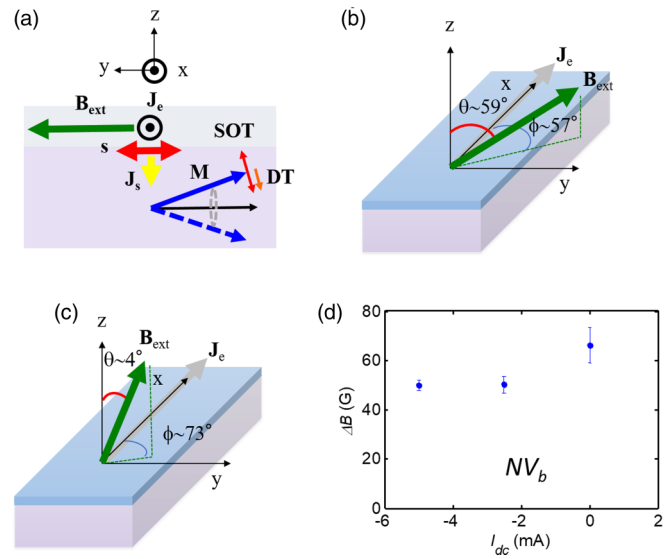

FIG. 9. SOT and its dependence on the relative orientation between injected spins and bias field. (a) Assuming the DC current $\mathbf{J_e}$ is along the long direction of the device (x axis), a spin current is sent along the vertical, z direction. The injected spins are necessarily oriented along the short direction (y axis) of the device. Therefore, the ideal orientation of the bias field B_{ext} is along the y direction, as then the YIG magnetization $\mathbf{M}$ (in the absence of excitation) is parallel to the orientation of the injected spins $\mathbf{s}$. This leads to the maximal spin-orbit torque (SOT) available. The SOT can act either along or against the damping torque (DT), depending on the orientation of injected spins, which is set by the direction of the DC current. (b) Orientation of the NV, and hence $\mathbf{B}_{\text{ext}}$, employed in single-spin sensing in this work (NV_a). The projection of $\mathbf{B}_{\text{ext}}$ on the y axis is $\sim 0.72|\mathbf{B}_{\text{ext}}|$. (c) Orientation of another NV (NV_b) present in the nanobeam. The projection of the corresponding $\mathbf{B}_{\text{ext}}$ on the y axis is $\sim 0.08|\mathbf{B}_{\text{ext}}|$. (d) Influence of I_{dc} on SW linewidth measured via NV spin-relaxometry [similar to those shown in main text Fig. 5(b)] but now with NV_b.

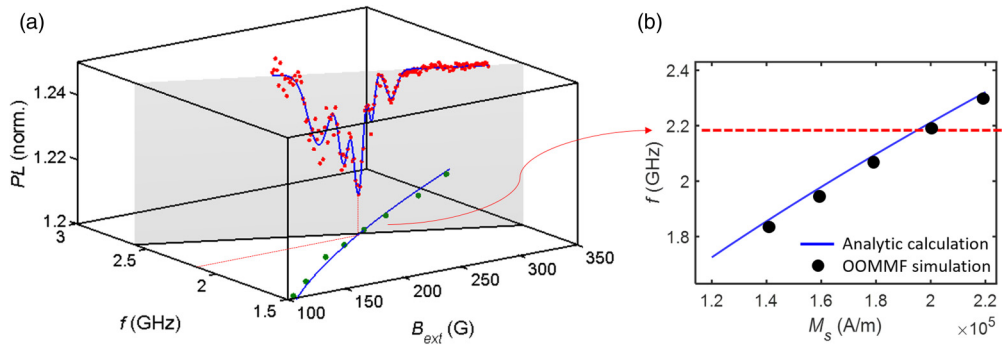

FIG. 10. Determination of saturation magnetization (M_s). (a) NV spin-relaxometry measurements at $I_{dc} = 0$ on $m_s = 0 \leftrightarrow -1$ transition over a wide range of B_{ext} (red dots on gray vertical plane). The bottom plane of the figure including green dots showing center frequency of the fundamental SW mode, a blue trace showing a fit to the green dots, and black line indicating the NV $m_s = 0 \leftrightarrow -1$ transition, is reproduced from main text Fig. 1(e). The strongest NV spin-relaxometry resonance dip at $I_{dc} = 0$ corresponds to the crossing point of the NV $m_s = 0 \leftrightarrow -1$ transition and the fundamental mode of the Pt/YIG microstructure at $B_{ext} = 245$ Gauss and $f = 2.18$ GHz. (b) To validate our analytical formalism to calculate M_s, a micromagnetic simulation (OOMMF) is performed at $B_{ext} = 245$ Gauss with different values of M_s. Simulation results (black dots) match very well with analytical calculation (blue line). Red dashed line corresponds to the frequency of the fundamental mode ($f = 2.18$ GHz) and the crossing point between this red dashed line and blue line determines the saturation magnetization M_s used throughout this work.

experimentally observed. In Fig. 9(d), we show linewidth measurements obtained from spin-relaxometry measurements using NV_b when $\mathbf{B}_{ext}$ is aligned with NV_b. Linewidth narrowing (observed in this case for current increasing in the negative direction) is discernible but much less significant than those measured with NV_a.

APPENDIX C: DETERMINATION OF SATURATION MAGNETIZATION (M_s)

We use the following methodology to determine M_s. First, we determine the fundamental mode, which is recognized based on two arguments:

(1) It is the strongest mode measured by NV stray-field magnetometry over a wide range of B_{ext} [shown as green dots in Fig. 10(a)].

(2) It corresponds to the strongest resonance dip measured by NV spin-relaxometry [red dots shown in Fig. 10a), where the frequency of this mode coincides with the frequency of the NV lower ($m_s = 0 \leftrightarrow -1$) transition [i.e., where the blue curve crosses the black curve in Fig. 10(a)].

This methodology provides strong evidence that the most prominent resonance observed in both measurements corresponds to the same mode: the fundamental (quasiuniform) SW mode, also known as FMR. A vertical red dashed line, which links data from these two different measurements, is drawn in Fig. 10(a) to illustrate such correspondence.

After recognizing the fundamental mode, we resort to an analytical approach to calculate M_s. Equations (45)–(48) from Ref. [45] are used to calculate the resonance frequencies of rectangular magnetic elements. A simple demagnetization factor is computed as in Ref. [46] by using the measured YIG microstructure dimensions. As B_{ext} is measured along the NV axis, a projected field [i.e., $B_{ext} * \sin(\theta)$, see Fig. 9(b) for definition of θ] is substituted as the external bias field throughout the equations. With this formalism, experimental data are fit with only one free parameter M_s: the blue line in the bottom plane of Fig 10(a) shows such a fit, from which we extract $M_s = 1.95(2) \times 10^5$ A/m. We note that determination of the saturation moment should be performed using a magnetometer in future work.

To validate this analytical calculation, we perform a micromagnetic (OOMMF [47]) simulation with the same material parameters at $B_{ext} = 245$ Gauss (along the NV axis). We find good agreements between the numerical simulation [black dots in Fig. 10(b)] and the analytical calculation (blue line).

APPENDIX D: IDENTIFICATION OF THE NATURE AND ORDER OF SW MODES

We use the following evidence to clarify the nature and order of the SW modes order of the SW modes (Table I).

(1) NV spin-relaxometry measurements clearly show five modes [designated as M_1, M_2, M_3, M_4, M_5, shown in Fig. 11(a)] that can be grouped into bulk modes and edge modes. More precisely, $M_1 \sim M_5$ corresponds to five 1D mode bands, where each band contains a series of modes quantized by the length of the YIG microstructure. We use the following arguments to identify the mode nature, i.e., bulk or edge.

(a) Bulk modes (particularly the fundamental mode, i.e., quasiuniform mode) are more susceptible to spin current than edge modes [48], because: (i) edge modes have larger inhomogeneous broadening, likely due to magnetic spatial inhomogeneities, such as edge roughness; (ii) usually charge current density is smaller near the edges due to enhanced electron scattering at the Pt/YIG device edge; and (iii) rotation of spin current polarization to the out-of-plane direction near the microstructure edge.

(b) At the same bias field, edge modes have lower energy than bulk modes, because of the reduced internal magnetic field near the microstructure edges [46].

(c) The same group of modes show similar SW spectra as a function of bias field [49].

Using these criteria, we attribute M_1, $M_2|_{I<2\,mA}$, $M_3|_{3<I<4.5\,mA}$, $M_4|_{I>5.5\,mA}$, and M_5 to a group of bulk modes;

TABLE I. Summary of SW mode identifications and auto-oscillation state. Here B stands for the bulk mode E for the edge mode. n is the bulk mode order, n' is the edge mode order. N.O. means not observed, while "-" means not in auto-oscillation state. M_x/M_y means mode hybridization between mode x and y.

Mode ID / I_{dc} (mA)	M_1		M_2		M_3		M_4		M_5	
-6 ∼ 2	B ($n = 2$)	–	B ($n = 1$)	–	E ($n' = 2$)	–	E ($n' = 1$)	–	N.O.	–
2 ∼ 3	B ($n = 2$)	–	M_2/M_3	–	M_2/M_3	–	E ($n' = 1$)	–	N.O.	–
3 ∼ 4.5	B ($n = 2$)	–	E ($n' = 2$)	–	B ($n = 1$)	STO_2	E ($n' = 1$)	–	N.O.	–
4.5 ∼ 5.5	B ($n = 2$)	STO_1	N.O.	–	M_3/M_4	STO_2	M_3/M_4	–	N.O.	–
5.5 ∼ 6	B ($n = 2$)	–	N.O.	–	E ($n' = 1$)	–	B ($n = 1$)	STO_2	B ($n = 3$)	–

and $M_2|_{I>3\,\mathrm{mA}}$, $M_3|_{I<2\,\mathrm{mA}}$, $M_4|_{I<4.5\,\mathrm{mA}}$ to a group of edge modes. We note the necessity to specify the current range for the nature of the modes, because mode hybridization transforms the mode nature when the current is varied.

(2) For the NV stray-field magnetometry measurement, a SW is driven by the applied MW field. As there is about 20% variation in the MW field magnitude across the wire width, it is expected that both odd-symmetry modes ($n = 1, 3, 5 \ldots$) and even-symmetry modes ($n = 2, 4, 6 \ldots$) are excited. According to this assumption and the measured ∼85 MHz difference between M_1 and M_3 with stray-field magnetometry at 4.5 mA, we conclude that these two bulk modes correspond to $n = 2$ and 1, respectively.

(3) Our micromagnetic simulation shows that the bulk modes ($n = 1, 2, 3$) and edge modes ($n' = 1, 2$) correspond well to $M_{1\sim5}$ at $I_{dc} = 0$, as observed in NV spin-relaxometry measurements [shown in Fig. 11(b)]. The frequency spacing between adjacent modes is about 80 MHz, from NV stray-field magnetometry measurements, which also agree well with numerical simulation.

(4) Furthermore, the micromagnetic simulation also gives the SW magnetization spatial profiles of eigenmodes. The mode nature and mode order are evident by observing the spatial distribution of the local susceptibility (shown in Fig. 12).

APPENDIX E: ESTIMATE OF MODE COUPLING STRENGTH

To estimate the coupling strength, we first note that if two modes have angular frequencies ω_1, ω_2 in the absence of coupling, then in the presence of coupling with strength g, the eigenfrequencies are $f_1, f_2 = [w_1 + w_2 \pm (4g^2 + (w_1 - w_2)^2)^{1/2}]/2\pi$. Therefore, our first task is to determine frequencies for the mode dispersion from the data shown in Figs. 4(d) and 4(e).

The location of the mode in parameter space (B, I_{dc}), as obtained from an NV spin-relaxometry measurement, is the intersection of the surface of the SW dispersion $f_{SW}(B, I_{dc})$ with that of the NV (lower) transition frequency $f_{NV}(B, I_{dc})$. That is, the data (B, I_{dc}), e.g., as shown in Fig. 4(e), must satisfy

$$f_{1,2}(B, I_{dc}) = f_{NV}(B, I_{dc}). \tag{E1}$$

Then, to determine the frequency of each of these points, we simply need to know the corresponding NV transition frequency. The dependence of the NV transition frequency on B_{ext} (external bias field) and I_{dc} is decoupled; and hence we can write

$$f_{NV}(B, I_{dc}) = f_{NV}(B) + f_{NV}(I_{dc}) = D_{gs} - \gamma B + f_{NV}(I_{dc}), \tag{E2}$$

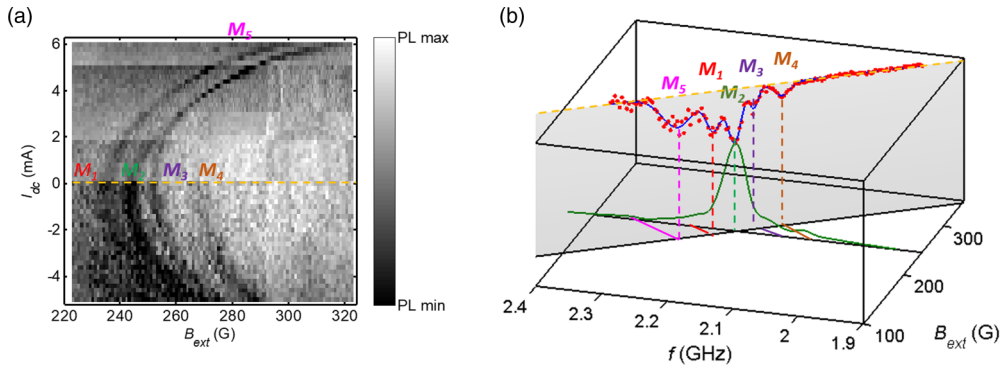

FIG. 11. SW mode designation and micromagnetic simulation (OOMMF). (a) This figure is reproduced from main text Fig. 4(c) with SW mode labeled as $M_1, M_2, \ldots, M_5$. (b) OOMMF simulation along with NV spin-relaxometry data [line cut from (a)] at $I_{dc} = 0$. Vertical plane (gray color shaded) can be projected onto the NV $m_s = 0 \leftrightarrow -1$ transition frequency (black diagonal line on the bottom plane). Relaxometry data (red points) and fit (blue line) are in this vertical plane; and the resonance dip can thus be projected onto the NV transition frequency connected via color-coded dashed lines (with the same color as the label of the corresponding mode). Green solid line is OOMMF simulation at bias field of 245 G (along NV axis). Resonance peaks (bulk mode $n = 1, 2, 3$; edge modes $n' = 1, 2$) are visible in simulation. Solid color-coded lines on the bottom plane show well-recognized correspondence between simulated resonance peaks and resonance dips measured with NV spin-relaxometry.

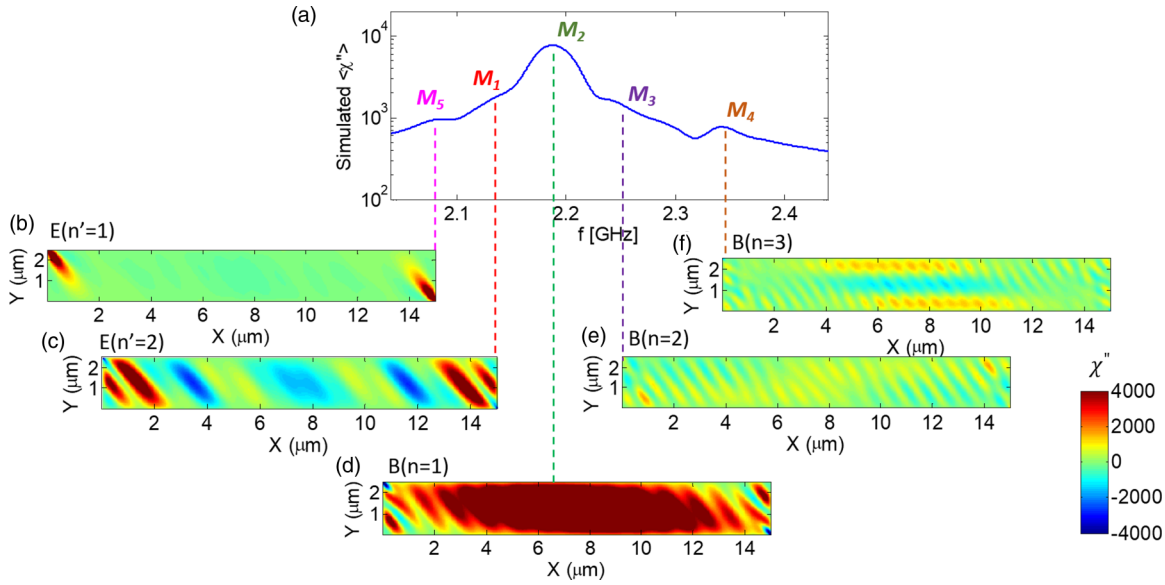

FIG. 12. Micromagnetic simulation (OOMMF) of SW spectrum and spatial magnetization profiles for different eigenmodes. (a) OOMMF simulated spectrum (performed at 245 G bias field along NV axis). Vertical axis represents spatially averaged magnetic susceptibility (imaginary part), $\langle\chi''\rangle$. (b) and (c) At $f = 2.08$ and 2.14 GHz, map of simulated local susceptibility (imaginary part), χ'', shows an edge mode localized at the corner of YIG microstructure. (d)–(f) At $f = 2.18$, 2.26, and 2.36 GHz, map of simulated local susceptibility (imaginary part), χ'', shows bulk mode sustained over entire YIG microstructur(e) with mode order $n = 1, 2, 3$ respectively. All spatial mode profile maps use the same color scale (right bottom color bar).

where D_{gs} is the NV zero field splitting, and γ is the NV gyromagnetic ratio. $f_{NV}(I_{dc})$ can be obtained at any bias field from NV electron spin resonance measurements at varying currents, i.e., via ODMR [Fig. 13(a)]. A linear + quadratic fit captures the dependence of the NV transition frequency on the current. We attribute the quadratic (symmetric) part to Joule heating, while the linear part may be attributed to the combined effect of the Oersted field generated by the current in the Pt and a change in magnetization caused by spin injection. The fit (excluding the constant term) gives

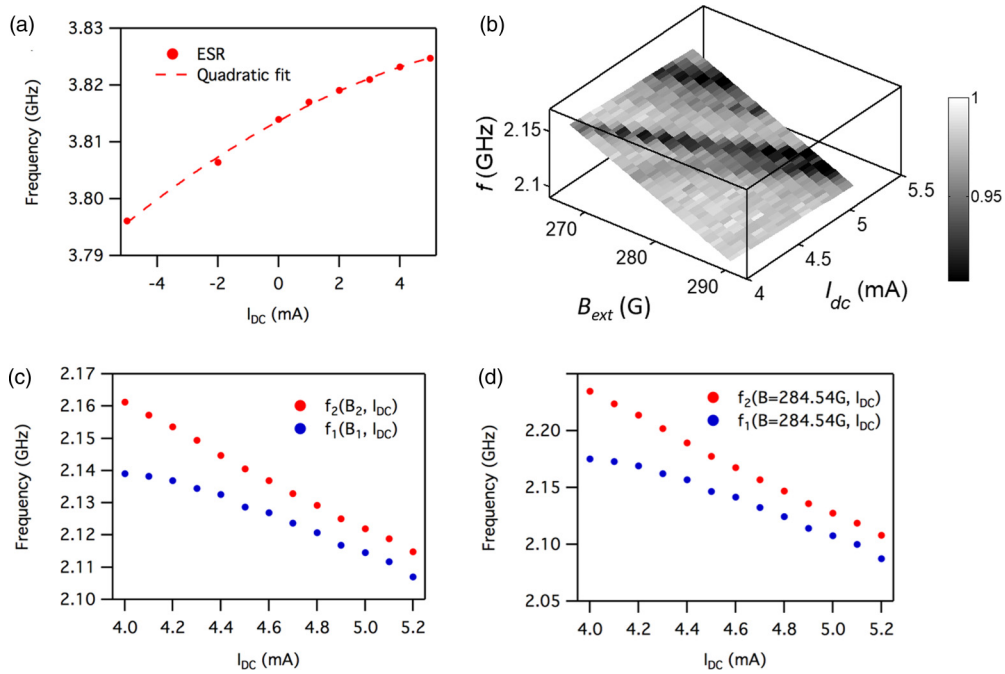

FIG. 13. Estimate of mode hybridization coupling strength. (a) Measured NV upper transition frequencies at 337 G as a function of DC current. The data is fit to a quadratic function (as well as smaller linear and constant terms). (b) NV spin-relaxometry data [from Fig. 4(e)] plotted at the plane of $f_{NV}(B, I_{dc})$. (c) Frequency value associated with each mode center $(B_{1,2}, I_{dc})$ from (b). (d) Dispersion at a fixed field ($B = 284.54$ G) as a function of the DC current.

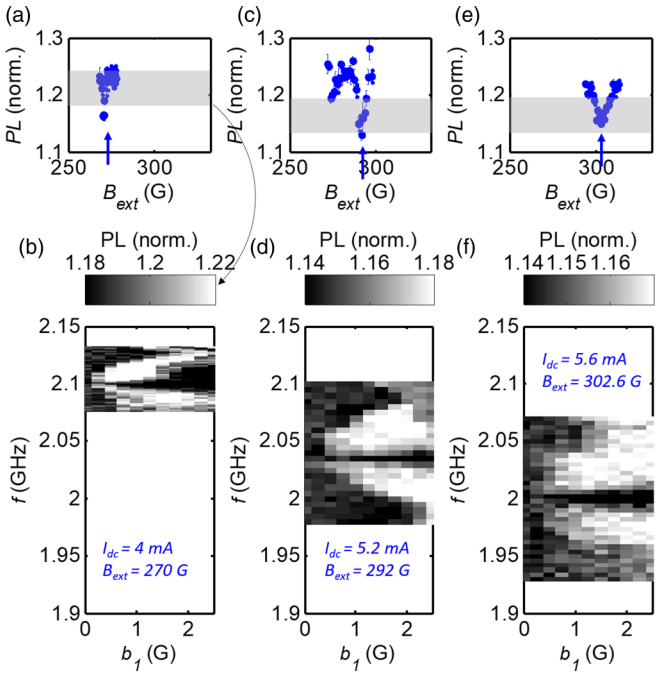

FIG. 14. STO_1 synchronization test to understand I_{dc} range of auto-oscillation and extract synchronization frequency interval. (a) NV PL vs field sweep [similar measurements as in main text Fig. 4(b)] at $I_{dc} = 4$ mA to find mode resonance as indicated by blue arrow. (b) At $I_{dc} = 4$ mA and $B_{ext} = 270$ G (mode resonance matching NV transition frequency), we perform 2D sweeping of the MW driving frequency and amplitude and simultaneously record the corresponding NV PL signal. This measurement is the same as that performed in Fig. 6. Here the 2D plot color bar corresponds to the PL level shaded by gray color shown in (a) and a dashed arrow is used to illustrate such correspondence. (c) and (e) show the same field sweep as in a but at different values of I_{dc} : 5.2 and 5.6 mA, respectively. (d) and (f) show a similar 2D plot but with different values of both I_{dc} : 5.2 and 5.6 mA and $B_{ext} = 292$ and 302.6 G.

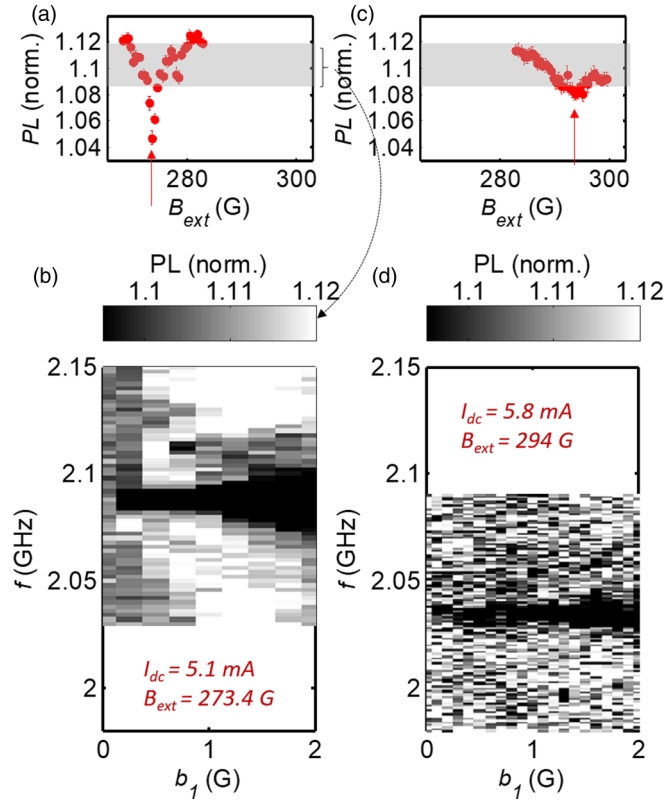

FIG. 15. Characterization of STO_2 by testing synchronization to external MW signals. (a) NV PL vs field sweep at $I_{dc} = 5.1$ mA to find center frequency of free running STO_2, as indicated by red arrow. (b) At $I_{dc} = 5.1$ mA and $B_{ext} = 273.4$ G, we perform 2D sweeping of the MW driving frequency and amplitude, and simultaneously record the corresponding NV PL signal. 2D plot color bar corresponds to the PL level covered by the gray shaded region shown in (a) and a dashed arrow is used to illustrate such correspondence. (c) Similar measurement as in (a) but at $I_{dc} = 5.8$ mA, and mode resonance takes place at $B_{ext} = 294$ G. (d) At $I_{dc} = 5.8$ mA, and $B_{ext} = 294$ G, we perform synchronization test measurements. No discernible signal contrast is observed.

$f_{NV}(I_{dc})$, with which we can determine $f_{1,2}(B_{1,2}, I_{dc})$, where $(B_{1,2}, I_{dc})$ are the locations of the modes as determined in Fig. 4(c). For better visualization, in Fig. 13(b) we also plot the measured two-dimensional (2D) NV PL signal on a surface defined by $f_{NV}(B, I_{dc})$, to reflect the fact that the probing frequency (i.e., f_{NV}) changes during 2D sweeping. In Fig. 13(c), we show $f_{1,2}$ determined from the measurements in Fig. 13(b).

The modes in the presence of coupling are given by

$$f_1, f_2 = [\omega_1(B, I_{dc}) + \omega_2(B, I_{dc}) \pm (4g^2 + ((\omega_1(B, I_{dc}) - \omega_2(B, I_{dc}))^2)^{1/2}]/2\pi \quad \text{(E3)}$$

Hence, if we have f_1, f_2 at the same (B, I_{dc}), we can find the squared difference $(f_1\text{-}f_2)^2$, and the minimum of this difference gives $4g^2$. Note that in Fig. 13(c), the pair of values f_1, f_2 at the same DC current is at different field values. As we want to determine frequencies for the mode dispersion for a fixed value of B_0, we linearize the dispersion:

$$f_{SW}(B_0 + \Delta B, I_{dc}) \sim f_{SW}(B_0, I_{dc}) + f_B(B_0, I_{dc})\Delta B, \quad \text{(E4)}$$

where f_B is the partial derivative of f with respect to B. For simplicity, we assume $f_B(B_0, I_{dc})$ is independent of the current, and hence we simply determine $f_B(B_0, I_{dc})$ from the Kittel-like dispersion at zero current. Then, we can construct f_1, f_2 at a fixed B_0, with the example shown in Fig. 13(d), which can readily be visualized in Fig. 13(b), as intersection points between the vertical plane, i.e., (f, I_{dc}) and each SW dispersion defined in plane of (f, B_{ext}). The minimum of the squared difference of these two dispersions then give us the coupling strength.

Using this approach for the hybridization near 2.2 mA, we obtain $g = 10$ MHz; and for the hybridization near 5 mA, we obtain $g = 9$ MHz.

APPENDIX F: STO SYNCHRONIZED TO EXTERNAL MW SOURCE (MEASUREMENT DETAILS)

As stated in the main text, we perform a modified NV spin-relaxometry measurement [illustrated in main text Fig. 6(a)] to test whether spectral features, those designated as STOs

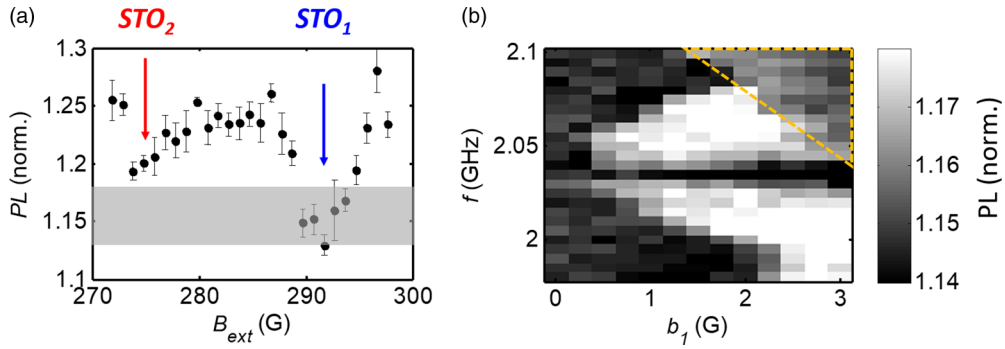

FIG. 16. Coexistence of STOs and their competing synchronization to external MW source. (a) At $I_{dc} = 5.2$ mA, NV PL vs field sweep shows two resonance peaks, which correspond to STO_2 (lower field) hence higher frequency) and STO_1. (b) At $I_{dc} = 5.2$ mA and $B_{ext} = 292$ G, synchronization test shows a parameter space area with an interesting signal feature surrounded by dashed yellow triangle.

(shown in Fig. 4), can be synchronized to an external MW drive. Such synchronization is evidence to distinguish unambiguously whether these spectral features are dominantly in an auto-oscillation state or in a thermal fluctuation state. We first find the frequency center of STO_1 by sweeping the bias magnetic field at a particular I_{dc} [e.g., $I_{dc} = 4$ mA, as in Fig. 14(a)]. Then we perform synchronization test by sweeping the driving MW field frequency/amplitude and recording NV PL signal. Figure 14(b) clearly shows the synchronization behavior: a bright PL region around the NV lower transition frequency indicates that the STO is now detuned from the NV lower transition frequency due to STO resonance synchronization to the external MW drive. Furthermore, the frequency interval of this region gradually increases as the driving amplitude increases. We pay attention to thresholding the PL signal to properly extract the synchronization frequency interval (Δf_s). More specifically, in the 2D plot, the PL upper limit is thresholded slightly below the background PL level, and the PL lower limit is thresholded above the PL level at the resonance dip. The gray color shaded area in Fig. 14(a) illustrates such thresholding limits. From these tests, we confirm that STO_1 is in an auto-oscillation state at least from $I_{dc} \approx 4$ mA to 5.6 mA.

A similar synchronization test performed with STO_2 (Fig. 15) shows that it is in an auto-oscillation state at $I_{dc} = 5.1$ mA, but in a thermal fluctuation state at $I_{dc} = 5.8$ mA.

STO coexistence is a common phenomenon for magnetic systems supporting a series of SWs. As evident in main text Fig. 4 and the aforementioned synchronization tests, STO coexistence does take place in our system. A summary of relevant observations is noted here. Figure 16(a) shows, at $I_{dc} = 5.2$ mA, by sweeping the bias field, both STO_1 and STO_2 are prominent. Then by fixing $I_{dc} = 5.2$ mA and $B_{ext} = 292$ G (where the NV lower transition is at the frequency of free-running STO_1), a synchronization test is performed. Surprisingly, an area in parameter space [surrounded by the dashed rectangle as shown in Fig. 16(b)] is found with a PL signal level between the synchronized situation (high PL level) and free-running situation (low PL level). Indeed, this observation can be understood by considering that the MW field also synchronizes STO_2 (which is at about 100 MHz higher frequency than STO_1) and the power of free-running STO_1 is partially absorbed by synchronized STO_2. From our observation, it seems that STO_2 is more prone to synchronization and drains most of the applied energy at higher MW driving amplitude.

[1] A. V. Chumak, V. I. Vasyuchka, A. A. Serga, and B. Hillebrands, Nat. Phys. **11**, 453 (2015).
[2] N. Locatelli, V. Cros, and J. Grollier, Nat. Mater. **13**, 11 (2014).
[3] T. Chen, R. K. Dumas, A. Eklund, P. K. Muduli, A. Houshang, A. A. Awad, P. Dürrenfeld, B. G. Malm, A. Rusu, and J. Akerman, Proc. IEEE **104**, 1919 (2016).
[4] V. E. Demidov, S. Urazhdin, G. de Loubens, O. Klein, V. Cros, A. Anane, and S. O. Demokritov, Phys. Rep. **673**, 1 (2017).
[5] J. Torrejon, M. Riou, F. A. Araujo, S. Tsunegi, G. Khalsa, D. Querlioz, P. Bortolotti, V. Cros, K. Yakushiji, A. Fukushima, H. Kubota, S. Yuasa, M. D. Stiles, and J. Grollier, Nature (London) **547**, 428 (2017).
[6] M. Collet, X. de Milly, O. d'Allivy Kelly, V. V. Naletov, R. Bernard, P. Bortolotti, J. Ben Youssef, V. E. Demidov, S. O. Demokritov, J. L. Prieto, M. Muñoz, V. Cros, A. Anane, G. de Loubens, and O. Klein, Nat. Commun. **7**, 10377 (2016).
[7] M. B. Jungfleisch, W. Zhang, J. Sklenar, J. Ding, W. Jiang, H. Chang, F. Y. Fradin, J. E. Pearson, J. B. Ketterson, V. Novosad, M. Wu, and A. Hoffmann, Phys. Rev. Lett. **116**, 057601 (2016).
[8] V. E. Demidov, M. Evelt, V. Bessonov, S. O. Demokritov, J. L. Prieto, M. Muñoz, J. Ben Youssef, V. V. Naletov, G. de Loubens, O. Klein, M. Collet, P. Bortolotti, V. Cros, and A. Anane, Sci. Rep. **6**, 32781 (2016).
[9] M. Montazeri, P. Upadhyaya, M. C. Onbasli, G. Yu, K. L. Wong, M. Lang, Y. Fan, X. Li, P. Khalili Amiri, R. N. Schwartz, C. A. Ross, and K. L. Wang, Nat. Commun. **6**, 8958 (2015).
[10] S. O. Demokritov, V. E. Demidov, O. Dzyapko, G. A. Melkov, A. A. Serga, B. Hillebrands, and A. N. Slavin, Nature (London) **443**, 430 (2006).
[11] J. R. Maze, P. L. Stanwix, J. S. Hodges, S. Hong, J. M. Taylor, P. Cappellaro, L. Jiang, M. V. G. Dutt, E. Togan, A. S. Zibrov, A. Yacoby, R. L. Walsworth, and M. D. Lukin, Nature (London) **455**, 644 (2008).

[12] M. S. Grinolds, M. Warner, K. De Greve, Y. Dovzhenko, L. Thiel, R. L. Walsworth, S. Hong, P. Maletinsky, and A. Yacoby, Nat. Nanotechnol. **9**, 279 (2014).

[13] K. Arai, C. Belthangady, H. Zhang, N. Bar-Gill, S. J. DeVience, P. Cappellaro, A. Yacoby, and R. L. Walsworth, Nat. Nanotechnol. **10**, 859 (2015).

[14] D. R. Glenn, D. B. Bucher, J. Lee, M. D. Lukin, H. Park, and R. L. Walsworth, Nature (London) **555**, 351 (2018).

[15] L. Rondin, J.-P. Tetienne, T. Hingant, J.-F. Roch, P. Maletinsky, and V. Jacques, Rep. Prog. Phys. **77**, 056503 (2014).

[16] A. Hamadeh, O. d'Allivy Kelly, C. Hahn, H. Meley, R. Bernard, A. H. Molpeceres, V. V. Naletov, M. Viret, A. Anane, V. Cros, S. O. Demokritov, J. L. Prieto, M. Muñoz, G. de Loubens, and O. Klein, Phys. Rev. Lett. **113**, 197203 (2014).

[17] M. J. Burek, N. P. de Leon, B. J. Shields, B. J. M. Hausmann, Y. Chu, Q. Quan, A. S. Zibrov, H. Park, M. D. Lukin, and M. Lončar, Nano Lett. **12**, 6084 (2012).

[18] T. X. Zhou, R. J. Stöhr, and A. Yacoby, Appl. Phys. Lett. **111**, 163106 (2017).

[19] L. Xie, T. X. Zhou, R. J. Stöhr, and A. Yacoby, Adv. Mater. **30**, 1705501 (2018).

[20] T. van der Sar, F. Casola, R. Walsworth, and A. Yacoby, Nat. Commun. **6**, 7886 (2015).

[21] N. Bar-Gill, L. M. Pham, A. Jarmola, D. Budker, and R. L. Walsworth, Nat. Commun. **4**, 1743 (2013).

[22] F. Casola, T. van der Sar, and A. Yacoby, Nat. Rev. Mater. **3**, 17088 (2018).

[23] A. Solyom, Z. Flansberry, M. A. Tschudin, N. Leitao, M. Pioro-Ladrière, J. C. Sankey, and L. I. Childress, Nano Lett. **18**, 6494 (2018).

[24] J. C. Slonczewski, J. Magn. Magn. Mater. **159**, L1 (1996).

[25] M. Bailleul, R. Höllinger, and C. Fermon, Phys. Rev. B **73**, 104424 (2006).

[26] V. E. Demidov, S. Urazhdin, E. R. J. Edwards, M. D. Stiles, R. D. McMichael, and S. O. Demokritov, Phys. Rev. Lett. **107**, 107204 (2011).

[27] V. M. Acosta, E. Bauch, M. P. Ledbetter, A. Waxman, L.-S. Bouchard, and D. Budker, Phys. Rev. Lett. **104**, 070801 (2010).

[28] H. A. Algra and P. Hansen, Appl. Phys. A **29**, 83 (1982).

[29] C. S. Wolfe, V. P. Bhallamudi, H. L. Wang, C. H. Du, S. Manuilov, R. M. Teeling-Smith, A. J. Berger, R. Adur, F. Y. Yang, and P. C. Hammel, Phys. Rev. B **89**, 180406(R) (2014).

[30] C. Du, T. van der Sar, T. X. Zhou, P. Upadhyaya, F. Casola, H. Zhang, M. C. Onbasli, C. A. Ross, R. L. Walsworth, Y. Tserkovnyak, and A. Yacoby, Science **357**, 195 (2017).

[31] V. E. Demidov, S. Urazhdin, H. Ulrichs, V. Tiberkevich, A. Slavin, D. Baither, G. Schmitz, and S. O. Demokritov, Nat. Mater. **11**, 1028 (2012).

[32] A. Slavin and V. Tiberkevich, IEEE Trans. Magn. **45**, 1875 (2009).

[33] A. Hamadeh, G. de Loubens, V. V. Naletov, J. Grollier, C. Ulysse, V. Cros, and O. Klein, Phys. Rev. B **85**, 140408(R) (2012).

[34] V. E. Demidov, H. Ulrichs, S. V Gurevich, S. O. Demokritov, V. S. Tiberkevich, A. N. Slavin, A. Zholud, and S. Urazhdin, Nat. Commun. **5**, 3179 (2014).

[35] W. H. Rippard, M. R. Pufall, S. Kaka, T. J. Silva, S. E. Russek, and J. A. Katine, Phys. Rev. Lett. **95**, 067203 (2005).

[36] J. F. Barry, J. M. Schloss, E. Bauch, M. J. Turner, C. A. Hart, L. M. Pham, and R. L. Walsworth, Rev. Mod. Phys. **92**, 015004 (2020).

[37] S. Tamaru, H. Kubota, K. Yakushiji, S. Yuasa, and A. Fukushima, Sci. Rep. **5**, 18134 (2016).

[38] M. Collet, O. Gladii, M. Evelt, V. Bessonov, L. Soumah, P. Bortolotti, S. O. Demokritov, Y. Henry, V. Cros, M. Bailleul, V. E. Demidov, and A. Anane, Appl. Phys. Lett. **110**, 092408 (2017).

[39] B. Sutton and S. Datta, Sci. Rep. **5**, 17912 (2016).

[40] C. Safranski, I. Barsukov, H. K. Lee, T. Schneider, A. A. Jara, A. Smith, H. Chang, K. Lenz, J. Lindner, Y. Tserkovnyak, M. Wu, and I. N. Krivorotov, Nat. Commun. **8**, 117 (2017).

[41] T. Giamarchi, C. Rüegg, and O. Tchernyshyov, Nat. Phys. **4**, 198 (2008).

[42] M. Lang, M. Montazeri, M. C. Onbasli, X. Kou, Y. Fan, P. Upadhyaya, K. Yao, F. Liu, Y. Jiang, W. Jiang, K. L. Wong, G. Yu, J. Tang, T. Nie, L. He, R. N. Schwartz, Y. Wang, C. A. Ross, and K. L. Wang, Nano Lett. **14**, 3459 (2014).

[43] M. B. Jungfleisch, V. Lauer, R. Neb, A. V. Chumak, and B. Hillebrands, Appl. Phys. Lett. **103**, 022411 (2013).

[44] J.-P. Tetienne, L. Rondin, P. Spinicelli, M. Chipaux, T. Debuisschert, J.-F. Roch, and V. Jacques, New J. Phys. **14**, 103033 (2012).

[45] C. Bayer, J. Jorzick, S. O. Demokritov, A. N. Slavin, K. Y. Guslienko, D. V. Berkov, N. L. Gorn, M. Kostylev, and B. Hillebrands, in *Spin Dynamics in Confined Magnetic Structures III*, edited by B. Hillebrands and A. Thiaville (Springer-Verlag, Berlin, 2006), pp. 57–103.

[46] A. Aharoni, J. Appl. Phys. **83**, 3432 (1998).

[47] M. J. Donahue and D. G. Porter, *OOMMF User's Guide, Version 1.0, Interagency Report NISTIR 6376* (National Institute of Standards and Technology, Gaithersburg, MD, 1999).

[48] Z. Duan, C. T. Boone, X. Cheng, I. N. Krivorotov, N. Reckers, S. Stienen, M. Farle, and J. Lindner, Phys. Rev. B **90**, 024427 (2014).

[49] M. Bailleul, R. Höllinger, K. Perzlmaier, and C. Fermon, Phys. Rev. B **76**, 224401 (2007).